Coherent structures in wind shear induced wave–turbulence–vegetation interaction in water bodies

Tirtha Banerjee[a,*], Nikki Vercauteren[b], Marian Muste[c], Di Yang[d]

[a] Karlsruhe Institute of Technology (KIT), Institute of Meteorology and Climate Research (IMK-IFU), Garmisch-Partenkirchen, Bavaria 82467, Germany
[b] Department of Mathematics and Computer Sciences, Freie Universitaet Berlin, Berlin 14195, Germany
[c] Department of Civil and Environmental Engineering, IIHR Hydroscience and Engineering, The University of Iowa, Iowa City, IA 52242, USA
[d] Departmental of Mechanical Engineering, University of Houston, Houston, TX 77204, USA

ARTICLE INFO

ABSTRACT

Flume experiments with particle imaging velocimetry (PIV) were conducted recently to study a complex flow problem where wind shear acts on the surface of a static water body in presence of flexible emergent vegetation and induces a rich dynamics of wave–turbulence–vegetation interaction inside the water body without any gravitational gradient. The experiments were aimed at mimicking realistic vegetated wetlands and the present work is targeted to improve the understanding of the coherent structures associated with this interaction by employing a combination of techniques such as quadrant analysis, proper orthogonal decomposition (POD), Shannon entropy and mutual information content (MIC). The turbulent transfer of momentum is found to be dominated by organized motions such as sweeps and ejections, while the wave component of vertical momentum transport does not show any such preference. Reducing the data using POD shows that wave energy for large flow depths and turbulent energy for all water depths is concentrated among the top few modes, which can allow development of simple reduced order models. Vegetation flexibility is found to induce several roll type structures, however if the vegetation density is increased, drag effects dominate over flexibility and organize the flow. The interaction between waves and turbulence is also found to be highest among flexible sparse vegetation. However, rapidly evolving parts of the flow such as the air–water interface reduces wave–turbulence interaction.

1. Introduction

Flume experiments with particle imaging velocimetry (PIV) were conducted recently to mimic realistic wetlands where the water body is subjected to wind flow in the presence of flexible protruding vegetation without any gravitational gradient (Banerjee et al., 2015). Wind shear produces traveling waves on the water surface and the flexible vegetation are subjected to wind induced oscillations, the combination of which generates a rich and complicated dynamics inside the water body featuring wave–turbulence–vegetation interaction. The experiments were aimed at mimicking realistic wetlands and understanding this complicated interaction can help towards the development of better models for sediment and nutrient transport as well as greenhouse gas (such as methane and carbon dioxide) emission mechanisms from vegetated wetlands, which are important pieces in local and global carbon budgets. However, operational models for wetland flow use zeroth order models using an effective friction factor, which misses the intriguing and rich dynamics occurring throughout the depth of the fluid, which further motivates our study to uncover these interactions.
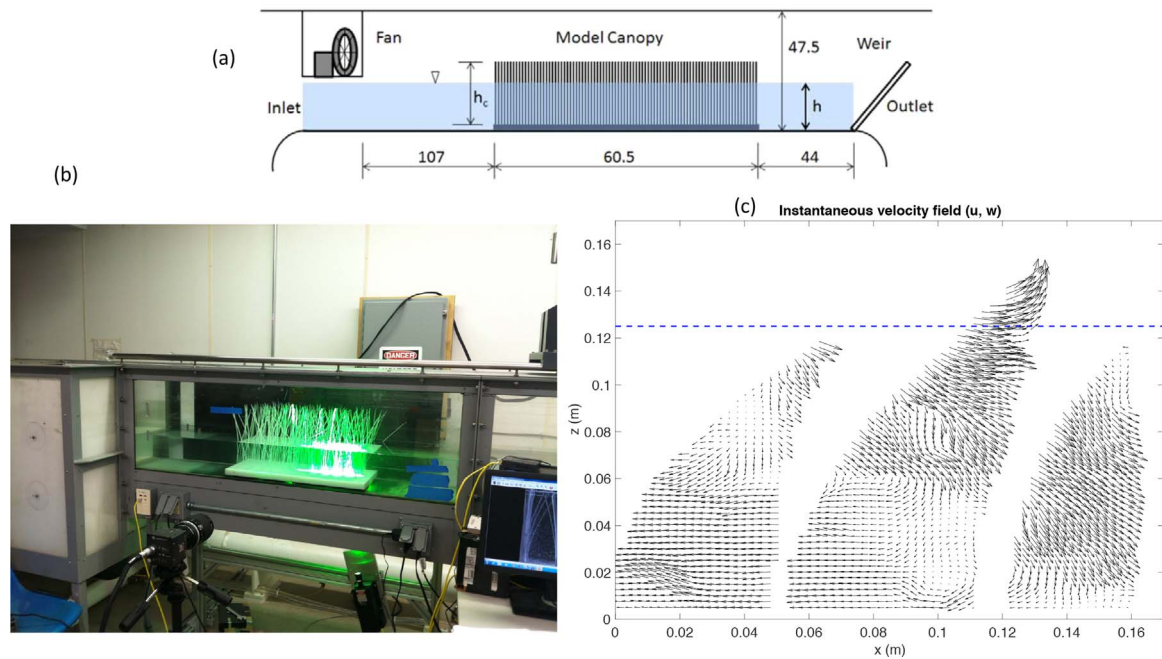
A large body of literature involving flow through vegetated channels and wetlands is reviewed in Banerjee et al. (2015) and not repeated here except the ones published between the years 2015–2016. Tse et al. (2016) reported experimental measurements both on air and water sides in presence of emergent vegetation and described how the "wind interacting with the vegetation generates coherent billows which are the dominant source of momentum into the wetland water column". Lal et al. (2015) found different flow regimes across depth in wetlands with dense emergent vegetation under wave forcing. Zhang et al. (2016) performed sensitivity studies for wave height, water depth and vegetation density in the context of wave–current–vegetation interaction in coastal waters. Several other studies also reported experimental and numerical modeling of flow through vegetated wetlands, focusing on sediment transport, flow attenuation and energy dissipation (Hu et al., 2015; Jin and Ji, 2015; Truong et al., 2015; Zhu and Chen, 2015; Carlin et al., 2016; Chakrabarti et al., 2016; Chen et al., 2016; Marsooli et al., 2016; Silinski et al., 2016; Tambroni et al., 2016; van Rooijen et al., 2016; Chao et al., 2016). However, most studies involving waves considered wave forcing on the whole body of fluid unlike in Banerjee et al.

Fig. 1. The top panel (a) shows a schematic of the experimental set up. The bottom panel (b) shows a picture snapshot of the experiment. The flume, the vegetation, the laser light sheet along with the illuminated area, the high speed camera and the image acquisition system can all be observed in the figure. Photo taken by the first author. Panel (c) shows an instantaneous velocity field for the flexible sparse scenario computed from PIV. The blue dashed line shows the water level for this case. (For interpretation of the references to color in this figure legend, the reader is referred to the web version of the article.)

(2015) and Tse et al. (2016) where wave action is generated on the air water interface because of wind shear. After Banerjee et al. (2015), only Tse et al. (2016) studied the full complexity of the interaction between wind shear, wave, turbulence and emergent vegetation to the best of the authors' knowledge.

Several factors such as wind speed, water depth, vegetation density and flexibility were found to influence the nature of this interaction as illustrated by first and higher order statistics obtained from separated wave and turbulence time series, the details of which can be found in Banerjee et al. (2015). All possible combinations of three different wind speeds (low, medium and high) and three different water depths (deep, intermediate and shallow) were tested for each of the five scenarios (with their abbreviations to be used throughout this article), i.e., no vegetation (NV), rigid sparse vegetation (RS), rigid dense vegetation (RD), flexible sparse vegetation (FS) and flexible dense vegetation (FD). As concluded in Banerjee et al. (2015), there are similarities between the no-vegetation scenario and an inverted boundary layer, in the sense that the air–water interface behaves like the wall in a regular boundary layer flow. Turbulence is generated by the disturbance at the interface and at sufficient depth, an extensive inertial subrange can be found. Wave motions are also generated at this interface in the form of rolling motions of impinging orbitals. These orbitals are damped deep inside the flow. The flexible dense vegetation adds vegetative drag in the mix and enhances fine scale inertial turbulence. The dominant wave frequency band of 4 Hz is found to be diffused by the oscillation of the vegetation between 2 and 5 Hz. The turbulent component of the momentum flux is found to be maximum at the middle depths, while in contrast, the wave component of the momentum flux is found to be maximum close to the air–water interface. The intensity (described as standard deviation of the streamwise and vertical velocity fluctuations) for wave and turbulence also display different behavior. The turbulence intensity is higher than wave intensity in all cases, and it also penetrates deeper into the flow than the wave intensity for larger flow depth scenarios. The wave intensity is highest close to the interface as well. The 'quasi-isotropic' nature of the flow is another interesting feature- meaning the vertical and longitudinal velocity components exhibit similar patterns of energy and momentum transfer. However, further

analyses are required to have a more detailed understanding of coherent structures in such a complicated flow, which encompasses the objective of this study.

Turbulent structures, also called quasi-coherent structures, are difficult to define precisely but have been described by Pope (2001) as "regions of space and time (significantly larger than the smallest flow or turbulent scales) within which the flow field has a characteristic coherent pattern". Kline and Robinson (1990) and Robinson (1991) categorized several types of coherent structures in channel and boundary layer flows, among which sweeps, ejections and vortical structures will be investigated in the present work. The relative contributions of sweeps and ejections in turbulent and wave momentum transfer will be studied. To study vortical motions, proper orthogonal decomposition (POD) will be conducted on the velocity fields. Furthermore, to study the degree of organization of the complex eddy motions and the interaction and exchange of information between wave and turbulence, some techniques from nonlinear dynamics such as Shannon entropy and mutual information content (MIC) will be employed as these methods "provide 'scalar measures' that can be related to the system's complexity (Wesson et al., 2003; Poggi et al., 2004)". To reveal the nature of the coherent structures in the context of this complex process, the present work aims at answering the following questions:

1. What is the dominant mode of vertical momentum transport for wave and turbulence and how is it affected by changes in water height, wind speed, vegetation density and flexibility?
2. How do the most energetic coherent structures look like for wave and turbulent transport of energy and momentum and what is the effect of water height, wind speed, vegetation density and flexibility on these features?
3. What is the degree of complexity and flow organization across the different scenarios and how is that affected by the control parameters such as water height, wind speed, vegetation density and flexibility?
4. How to quantify the interaction between wave and turbulence and how does it vary with the aforementioned control parameters?

2. Experiment

The experimental setup is discussed in Banerjee et al. (2015), however, some details are repeated here for the sake of completion. Panel (a) of Fig. 1 shows the schematic of the experimental set-up along with dimensions. Panel (b) of Fig. 1 shows an original snapshot of the experiment. Part of the flume is visible, along with the vegetation, the illumination of the flow field by the laser light sheet, the high speed camera and the image acquisition system. The dimensions of the flume were 211.5 cm in length, 35 cm in width and 47.5 cm in height. A fan with three different wind speeds was placed at the leftmost end of the flume on a platform that could be raised or lowered vertically with water height, so that the wind shear works just above the water surface. The vegetation was placed at the central section of the flume so there was minimum reflection of surface waves from the other end and the surface waves were fully developed. Moreover with the range of wind speeds (2.83 ms^{-1} (W1), 3.33 ms^{-1} (W2), 3.37 ms^{-1} (W3)), reflection effects were deemed minimal. The wind speeds were measured however with a hand held anemometer, so precise wind measurements were not available. Three different water heights (0.125 m (H1), 0.070 m (H2), 0.025 m (H3)) were used for each of the wind speed cases, so there were 9 wind speed-water height combinations for each of the five scenarios – no vegetation, rigid sparse, rigid dense, flexible sparse and flexible dense. The vegetation was simulated by nylon cable ties, which were 4 mm wide and 1 mm thick and were planted on a PVC test bed. Their full length of 27.3 cm was used to simulate the flexible cases. The same cable ties, when cut to about 7 cm, behaved quite rigidly. This was used to our advantage and used as rigid vegetation. This results in the fact that the rigid vegetation cases were actually submerged for the deepest depth case (H1). The vegetation density (λ_d) calculated based on the frontal area per area of the test bed were 0.39 for sparse and 1.04 for dense. Incidentally, a similar order of magnitude of non-dimensional vegetation density 0.15 was used by Tse et al. (2016) for sparse vegetation. In our experiment, the densities were selected carefully so that they still mimic realistic vegetated wetland scenarios, while still allowing enough open areas for imaging such that meaningful flow quantities can be obtained. As seen in the panel (c) of Fig. 1, which depicts an instantaneous snapshot of the velocity field calculated from PIV for the flexible sparse scenario with a H1W1 combination (taken from Banerjee et al. (2015)), about 60% of the field of view is unobstructed where flow quantities are available. For the PIV, a very thin laser light sheet was passed through a 1.5 mm slit carved at the bottom of the test bed. Small neutrally buoyant hollow glass spheres were used to seed the flow which illuminated the flow field in the path of the laser light sheet. As observed in panel (c) of Fig. 1, the field of view was about 15 cm by 15 cm. A high speed camera was used to image the flow field in 30 Hz frequency, while each run was filmed for 30 s, generating 900 images for every set. This combination of sampling frequency and the 30 s imaging time were deemed sufficient by trial and error since many wave cycles were observed to pass the region of interest. The seeding density was also determined by trial and error so that there were neither too less nor too many particles in a region of interrogation while computing spatial correlations in the PIV algorithm. However, the trial and error practices were not arbitrary and were guided by a few principles (Raffel et al., 2013) – that the interrogation region size was small enough so that one flow vector described the flow for that region, the maximum in-plane displacement was less than 1/4 of the interrogation region size, there were at least 10 particle image pairs per interrogation region and a particle occupied 3–6 pixels in the field of view, which was 1024 by 1024 pixels. The experimental conditions are listed in Table 1.

To have some estimate of the wave motion, the continuous fluctuations of the water levels were measured with a wave gauge for each of the three wind speeds. Fourier transforms of these water level fluctuations reveal a dominant wave frequency close to 4 Hz. Banerjee et al. (2015) presents further calculations of wave amplitudes, momentum

Table 1
Experimental conditions for the experiments.

Water depth (H) (m)	Wind speed (W) (m/s)
0.125	2.83
0.070	3.33
0.025	3.37

roughness heights using Charnock's equation and friction velocities on the air and water side to compare this experimental setup with realistic scenarios as found in natural wetland flows and it was concluded that "the flume experiments 'mimic' key aspects of wind dynamics and interfacial momentum transfer over large water bodies in nature despite the primitive wind generation mechanism and lateral edges of the flume". It is worth noting that the recent paper by Chao et al. (2016) found similar patterns in mean velocity, namely maximum velocity at the interface and counter-current flow at the bottom depending upon flow conditions, as well as turbulent intensity.

Once the velocity fields were calculated using the open source software PIVLab (Thielicke and Stamhuis, 2010), further data analysis were conducted to separate wave and turbulent motions. First the data were de-noised using a Lorenz curve type analysis the details of which can be found in Banerjee et al. (2015). The de-noised signals were then spectrally analyzed to extract the wave (as the deviation of the spectrum from the $-5/3$ scaling in the frequency band of 3–5 Hz) and turbulent components of the signals (Banerjee et al., 2015). These separated wave and turbulence signals will be used in the present work to explore coherent structures. As will be discussed later, the choice of methods to study coherent structures should reveal more insights above traditional ways of visualizing vorticity and Q criteria.

3. Data analysis

3.1. Sweeps and ejections

It was noted by Kline et al. (1967) that fluid motion close to the wall is far from being completely chaotic in nature and exhibits a sequence of ordered motions. The impact of such large scale organized motions on momentum transfer is often studied by conditional sampling and quadrant analysis Antonia (1981), Katul et al. (2006), Wallace (2016). Quadrant analysis refers to studying the joint scatter of the longitudinal velocity fluctuations (u') and the vertical velocity fluctuations (w') components. Assuming u' is the abscissa and w' is the ordinate, the covariance $\overline{u'w'}$, which represents the vertical momentum flux or Reynolds stress is conditionally sampled in one of the four quadrants of the $u' - w'$ coordinate system. The first quadrant, where $u' > 0$, $w' > 0$, and the third quadrant where $u' < 0$, $w' < 0$, contain the positive $\overline{u'w'}$ values. The second quadrant where $u' < 0$, $w' > 0$, and the fourth quadrant where $u' > 0$, $w' < 0$, contain the negative values of $\overline{u'w'}$. If the net vertical momentum transfer is negative or downward, ($\overline{u'w'} < 0$), (as is the case in canopy turbulence), events in quadrant II are called ejections and events in quadrant IV are called sweeps. The mode of momentum transfer in quadrant I is called outward interactions and events in quadrant III are called inward interactions. If the net vertical momentum flux is positive, these definitions are reversed. Table 2 summarizes these definitions. Nevertheless, the difference between the net

Table 2
Definition of sweep and ejection events.

Case	Event	Definition
$\overline{u'w'} < 0$	Sweep	$u' > 0$, $w' < 0$
$\overline{u'w'} < 0$	Ejection	$u' < 0$, $w' > 0$
$\overline{u'w'} > 0$	Sweep	$u' < 0$, $w' < 0$
$\overline{u'w'} > 0$	Ejection	$u' > 0$, $w' > 0$

sweep and ejection dominated vertical momentum transport relative to the net vertical momentum flux is defined as (Nakagawa and Nezu, 1977; Raupach, 1981)

$$\Delta S_0 = \frac{\overline{u'w'}_{\text{sweep}} - \overline{u'w'}_{\text{ejection}}}{\overline{u'w'}}. \tag{1}$$

Note that if $\Delta S_0 > 0$, then sweeps dominate momentum transfer and if $\Delta S_0 < 0$, then ejections dominate momentum transfer. Thus the non-dimensional parameter $-1 < \Delta S_0 < 1$ can be taken as an important measure of coherent structures since it describes the dominant mechanism of momentum transfer in a complicated flow. The variation of ΔS_0 across different experimental scenarios can reveal the nature of organized motions as they vary with water depth, wind speed and vegetation rigidity. It is also important to note that sweeps and ejections have been found to be the dominant turbulent momentum transfer mechanisms in atmospheric and canopy turbulence. Furthermore, the quantity $\Delta S_0 > 0$ has also been found to be related to turbulent triple moments such as skewness and mixed moments) (Katul et al., 2006; Wallace, 2016).

3.2. Proper orthogonal decomposition (POD)

Proper orthogonal decomposition (POD) has been described by Pope (2001) as an objective technique that identifies the most energetic flow structures in a flow field (Berkooz et al., 1993; Pope, 2001). In recent years, POD has become a very popular tool to study coherent structures in turbulent flows (Berkooz et al., 1993; Graftieaux et al., 2001; Smith et al., 2005; Caver and Meyer, 2012; Calaf et al., 2013; Chen et al., 2013; Tirunagari, 2015), which was originally used by Lumley (1967) to extract eddies with large length scales in shear flows (Chen et al., 2013). Different methods can be used for POD; however, the method of snapshots is ideal for PIV data (Graftieaux et al., 2001).

Conceptually, in a POD using the method of snapshots, a series of time instances of the flow is decomposed into a "set of orthonormal basis functions or modes, that span the given dataset in the most "optimal" way (Caver and Meyer, 2012)". Every set of two dimensional velocity fields at every instant of time $(u, w)_{i,j}^{(k)}$ can be called $V^{(k)}$, where i and j refer to integer indices of the spatial velocity distributions. For each of u and w, both i and j run from 1 to the number of grid points in each directions (63 for this experiment). There are 900 snapshots in time, so k, the snapshot index runs from 1 to 900 for each scenario. $V^{(k)}$ is decomposed into a linear combination of $M = 900$ numbers of spatial basis functions, which are called POD modes and denoted by ϕ_m:

$$V^{(k)} = \sum_{m=1}^{M} c_m^{(k)} \phi_m, \tag{2}$$

where $c_m^{(k)}$ are called coefficients. The kinetic energy of the system is maximized under the constraint of orthonormality of the basis functions $\phi_m(x, z)$. The solution of this constrained optimization problem yields eigenvectors as ϕ_m and the corresponding eigenvalues describe the energy contribution of each of the eigenvectors or POD modes. If the eigenvalues are sorted in the descending manner, the top few POD modes are found to contain most of the energy of the system. A set of scalar snapshots can also be decomposed using the same principles. Further mathematical details can be found in Chen et al. (2013) and are not repeated here. It is worth noting here that in the current work, the usage of POD is for the sake of visualizing vortical patterns in space which are the most energetic coherent structures and not for developing reduced order models (Podvin and Fraigneau, 2017). The variation between the top POD modes of the flow fields across the different scenarios can illustrate the effects of wind speed, water height vegetation density and vegetation rigidity on coherent structures. Reduced order modeling using POD is beyond the scope of the current work but will be attempted in future.

3.3. Shannon entropy and mutual information content (MIC)

Techniques based on nonlinear time series analysis were used by Wesson et al. (2003) and Poggi et al. (2004) to explore the magnitude and degree of nonlinearity of the interaction between larger and smaller scales within and above plant canopies. Wesson et al. (2003) used Shannon entropy and mutual information content (MIC) to assess, quantify and differentiate the "degree of organization of complex eddy motions in the canopy sublayer (CSL) and the atmospheric surface layer (ASL)" – the dynamics of which are quite different. Hence these techniques can be useful to characterize the degree of organization in the complex motion in this study. Shannon entropy or 'information entropy' is a topological measure of the structure of flows and is defined as described in Wesson et al. (2003)

$$I_S = -\sum_i p_i \ln p_i \tag{3}$$

where $p_i(i = 1, 2, ..., M)$ is a non-negative and normalized discrete probability distribution which has additive properties, i.e.,

$$p_i \geq 0; \quad \sum p_i = 1; \quad p_{i \cup j \cup ...} = p_i + p_j + ... \tag{4}$$

(Shannon, 1948; Wijesekera and Dillon, 1997; Wesson et al., 2003). For the probability distribution to represent a particular process such that the Shannon entropy reflects the process spectrum, the spectrum can be defined as a sequence $\Psi_i(i = 1, ..., M)$ of M numbers such that $M > 0$ and $p_i = \Psi_i(\Sigma_i \Psi_i)^{-1}$ (Wijesekera and Dillon, 1997).

A flat, white noise spectrum has the highest possible value of Shannon entropy,

$$\Psi_i = 1; \quad p_i = M^{-1}; \quad I_{Sf} = \ln(M), \tag{5}$$

so $0 < S_N = I_S/I_{Sf} < 1$ can be defined as a normalized Shannon entropy and this non-dimensionalization eliminates the uncertainties between different experimental conditions (Wesson et al., 2003). As a physical interpretation, it can be mentioned that a flow with a higher degree of complexity would exhibit a lower Shannon entropy than a more 'boring' flow with lower degree of complexity. Thus the canopy sublayer shows a lower Shannon entropy than the atmospheric surface layer (Wesson et al., 2003).

Mutual information content (MIC) is a measure obtained using Shannon entropy and it measures the dependence between two random variables from the perspective of information content, i.e., the measure of amount of information contained by one random variable about the other random variable. It is defined as

$$I(s, q) = \sum_{i,j} p_{ij}(s, q) \ln p_{ij}(s, q) - \sum_i p_i(s) \ln p_i(s) - \sum_j p_j(q) \ln p_j(q) \tag{6}$$

where the first term on the right hand side indicates the joint Shannon entropy between s and q and the second and third terms indicate Shannon entropy for s and q respectively. In the current context, the MIC between the wave and turbulence components can directly quantify the information exchange between them and thus provide a quantitative measure for wave–turbulence interaction.

4. Results and discussions

4.1. Dominant modes of momentum transfer

4.1.1. Observation

Fig. 2 shows spatially averaged (horizontally across every level) profiles of ΔS_0 computed for the turbulent component of the velocities. Every panel presents the horizontally averaged ΔS_0 for all five scenarios – namely NV, RS, RD, FS and FD. Panels (a), (b) and (c) present the deep (H1), intermediate (H2) and shallow (H3) h cases respectively for the low U_a (W1). Panels (d), (e) and (f) present the deep (H1), intermediate (H2) and shallow (H3) h cases respectively for the medium U_a case
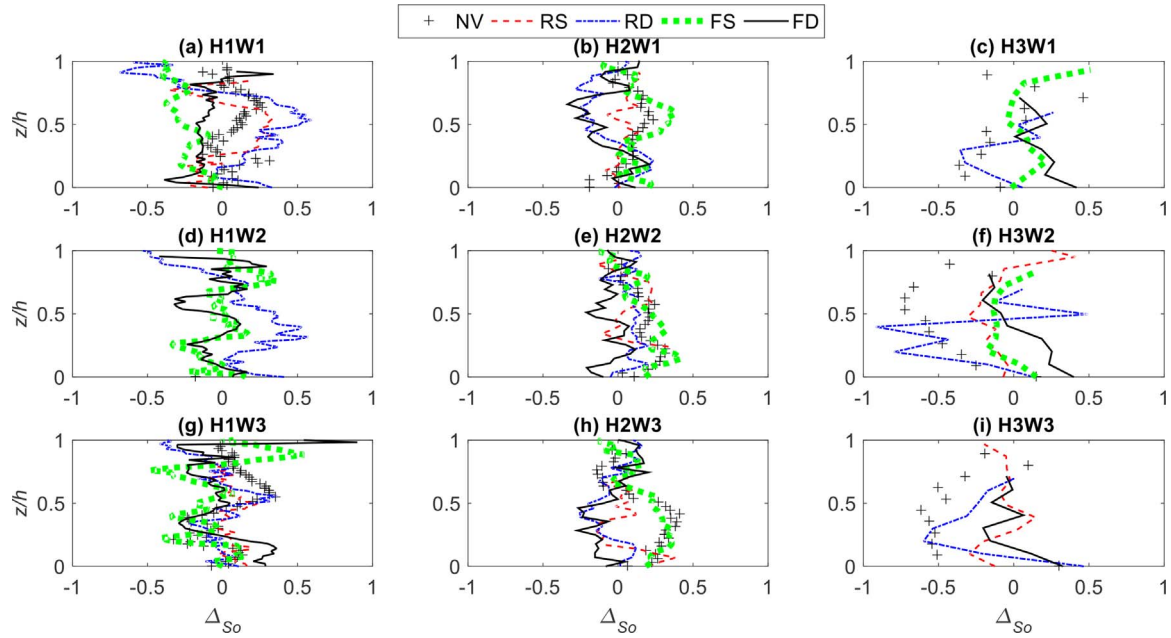
Fig. 2. Horizontally averaged ΔS_0, as a function of normalized height (z/h) using the turbulent component of the signals. Every panel presents $\Delta S_0(z)$ for the turbulent components for all five scenarios – namely no vegetation (black + symbols, NV), rigid sparse (red dashed line, RS), rigid dense (blue dash and dotted line, RD), flexible sparse (thick green dots, FS) and flexible dense (black line, FD). Panels (a)–(c) present the deep (H1), intermediate (H2) and shallow (H3) cases respectively for the low U_a case (W1). Panels (d)–(f) present the deep (H1), intermediate (H2) and shallow (H3) cases respectively for the medium U_a case (W2). Similarly, panels (g)–(i) present the deep (H1), intermediate (H2) and shallow (H3) cases respectively for the high U_a case (W3). Note that the RS case for panel (c), NV case in panel (d) and FS case in panel (i) are omitted for poor quality. (For interpretation of the references to color in this figure legend, the reader is referred to the web version of the article.)

(W2). Similarly, panels (g), (h) and (i) present the deep (H1), intermediate (H2) and shallow (H3) h cases respectively for the high U_a case (W3). The normalized height z/h is used in all data representations. Important observations from Fig. 2 are as follows:

1. The no-vegetation scenario (indicated by + symbols): For the deep and intermediate flow depth cases (i.e., H1 and H2, respectively), momentum transfer at most of the depth is sweep dominated except a small section in the middle which is weakly ejection dominated. The same behavior persists with increase of wind speed. For the shallow flow depth cases (H3), the no-vegetation cases are ejection dominated at most of the depth, with sweep-domination close to the air–water interface.

2. The rigid-sparse scenario (red dashed lines): Mostly sweep dominated for the deep water depth and the low wind case. In other cases, sweeps and ejections contribute more or less equally, except the shallow flow cases where ejection dominates.

3. The rigid-dense scenario (blue dash-dot lines): For the deep flow depth cases, momentum transfer is ejection dominated close to the air–water interface and sweep dominated at deeper depths. With shallower flow depths, the flow becomes more ejection dominated.

4. The flexible-sparse scenario (thick green dots): This is often opposite to the rigid vegetation scenario (dense and sparse). For the deep flow depth, the momentum transfer is ejection dominated especially for slower winds but becomes more sweep dominated for shallower flow depth cases.

5. The flexible-dense scenario (black line): This scenario is similar to flexible sparse cases where water depth is large. In intermediate depth cases, it is more similar to rigid dense cases, i.e., mostly ejection dominated. However, most shallow cases are generally sweep dominated.

4.1.2. Discussion

To summarize, for the deep flow depths, vegetation rigidity has more influence than vegetation density in separating turbulent momentum transfer mechanisms into sweeps and ejections, although this

differentiation becomes less prominent with faster wind speeds. For intermediate and shallow depths, the vegetation density seems to be the decisive factor for the dominating momentum transfer mechanism. This is probably because at H2 and H3 cases, the flow encounters the stems which are rigid even for flexible vegetation. It is interesting to note here that for atmospheric turbulence in dense plant canopies, momentum transfer is dominated by sweeps inside the canopy and ejections above the canopy; whereas for atmospheric turbulence in sparse canopies, ejections dominate momentum transfer both inside and above the canopy (Katul et al., 2006). For the wave component of the velocities, momentum transport has no clear sweep or ejection dominance (not shown), which is commensurate with wave dynamics – orbitals behave almost symmetrically and transfer momentum with both sweeps and ejections and also with inward and outward interactions (all of the four quadrants). To demonstrate this better one needs to look at the most energetic coherent structures under wave and turbulent motions, which is discussed in Section 4.2.

4.2. Visualizations of POD modes

4.2.1. Observation

The proper orthogonal decomposition technique is applied on both the wave and turbulent components of the velocity signals for all the scenarios in this work, but only a few interesting cases are discussed due to lack of space, where only the top three POD modes are shown along with their energy contents in parenthesis. Important observations from POD visualizations are listed below:

1. Fig. 3 shows the top 3 POD modes (quiver plots with the horizontal POD mode ϕ_x and the vertical POD mode ϕ_z) for the wave components of the no-vegetation scenario. The top row shows the top three wave modes (two dimensional) for the largest flow depth (H1), the middle row for intermediate depth (H2) and the last row for the shallowest flow (H3) – all for only the slowest velocity (W1). All panels are color-coded with the vertical POD mode (ϕ_z) so red indicates upward and blue indicates downward motion. The title of
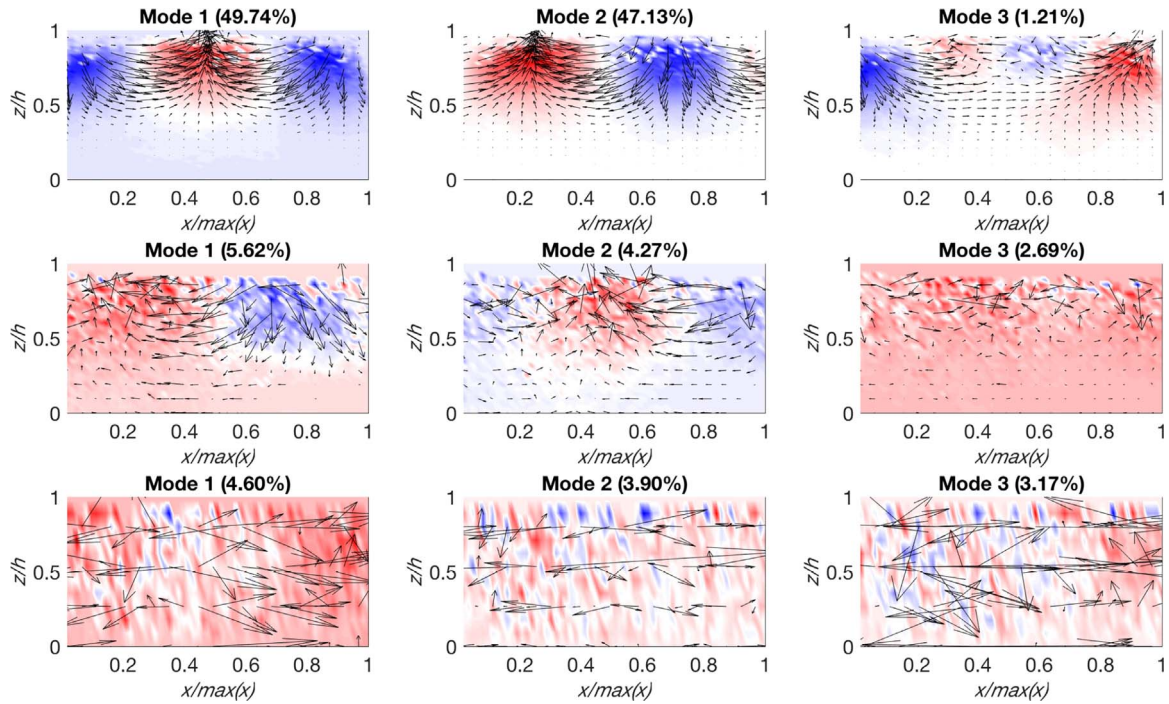
Fig. 3. Top 3 POD modes (quiver plots with the horizontal POD mode ϕ_x and the vertical POD mode ϕ_z) for the wave components of the no-vegetation scenario. The top row shows the top three wave modes (two dimensional) for the largest flow depth (H1), the middle row for intermediate depth (H2) and the last row for the shallowest flow (H3) – all for only the slowest velocity (W1). All panels are color-coded with the vertical POD mode (ϕ_z). The title of each panel mentions the energy content of that particular mode. The colormaps indicate the ϕ_z mode, lighter upward and darker downward. (For interpretation of the references to color in this figure legend, the reader is referred to the web version of the article.)

each panel mentions the energy content of that particular mode. The wave orbital motions briefly mentioned in Section 3.1 can be clearly observed here. The difference of the locations of wave orbitals in the top 3 modes for H1 (top panel) is also worth noting. The first mode shows two wave orbitals converging at the middle. The second mode shows one converging and one diverging node for three different wave orbitals. The third mode shows one larger orbital spanning the entire domain. With reduction of water depth, this degree of coherence gradually disappears as can be observed in the middle (H2) and bottom rows (H3). This loss of coherence is also reflected in the energy contents of the top 3 modes as the water height decreases.

2 The variation of energy content among the top POD modes across different scenarios is further illustrated by Fig. 4, where the cumulative energy contents of the top 150 wave-modes are plotted for the three depth cases (H1, H2 and H3) for the no-vegetation scenario as discussed in Fig. 3. In the deepest case in the top row (H1), top 2 modes contain about 97% of the wave kinetic energy while for the intermediate and shallow depth cases (middle row- H2 and bottom row-H3), the top 3 modes contain about 11–13% of the total wave kinetic energy and it takes about 150 modes to reach about 100% of the total wave kinetic energy.
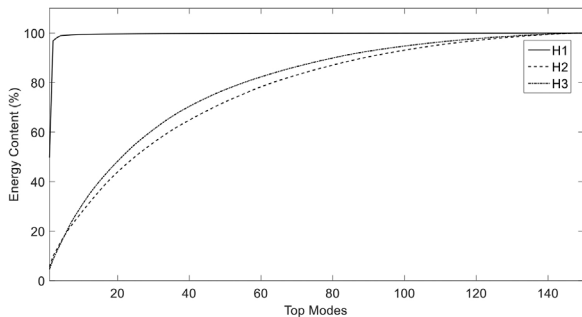
Fig. 4. Cumulative energy contents of the top 150 wave-modes are plotted for the three depth cases (H1, H2 and H3) for the no-vegetation scenario as discussed in Fig. 3.

3 Fig. 5 shows the top 3 POD modes for the turbulent component for the no-vegetation scenario, similarly as Fig. 3 for H1 (top), H2 (middle) and H3 (bottom row) cases (all for the slowest wind W1). It is interesting to note that the relative energy content (of the total turbulent energy) of the top 3 turbulent modes are much more than their wave counterparts (relative to the total wave energy), especially for the intermediate and shallow flow cases (middle and bottom row).

4 To study the influence on coherent structures by the addition of flexible sparse vegetation, top 3 turbulence POD modes are plotted in the same way in Fig. 6. The addition of vegetation introduces different structures than the no vegetation scenario. The top POD mode displays more of a advective (more parallel streamlines) structure. However several local roll type structures indicated by turning arrows and adjacent red-blue patches are visible throughout the depth for both the highest and intermediate depth scenarios.

5 When the density of vegetation is increased, this increased drag force further organizes the flow as evident from the top 3 turbulent POD modes for the flexible-dense scenario plotted in Fig. 7. Essentially most of the flow structures become advective in this scenario.

6 Fig. 8 shows the top 3 POD modes for the wave momentum transport, computed using snapshots of $u'w'$ for the no vegetation scenario along with contour lines. The POD modes for the deep flow conditions (H1) look quite distinct and different from the corresponding modes in Fig. 3 computed from energy considerations. For intermediate and shallow cases, the wave momentum modes lose all coherence.

4.2.2. Discussion

The loss of coherence with reduction of water height is an important observation. This is due to the transition from deeper waves to shallow waves ($h = 0.125$ m $> \lambda_w/2 = 0.038$ m for H1 but $h = 0.025$ m $< \lambda_w/2 = 0.038$ m for H3 cases, where $\lambda_w = 0.076$ m is the average wavelength for all three wind cases (Yang, 2001; Banerjee et al., 2015)) and a more efficient randomization of the wave energy because of the
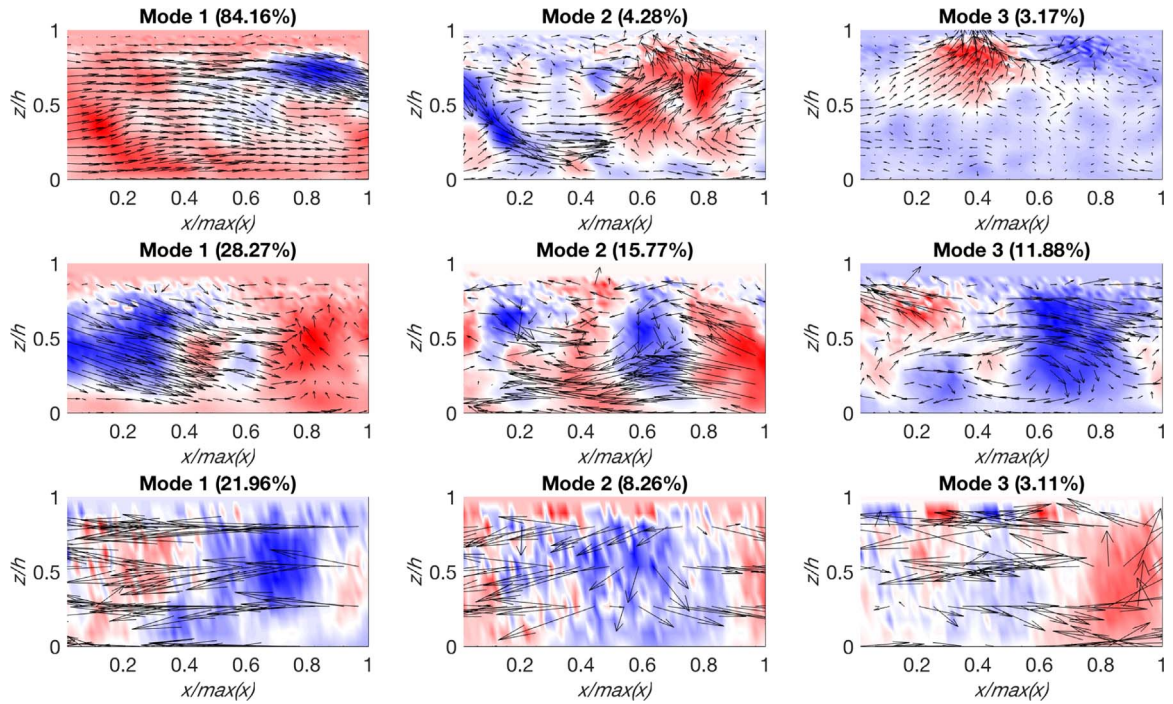
T. Banerjee et al.

Fig. 5. Same as Fig. 3 – top 3 POD modes but for the turbulence component in the no-vegetation scenario.

influence of the bottom surface. Although the strongest turbulent coherent structures are advective in nature, the oscillation of the vegetation short-circuits energy from air to water and the oscillation of the vegetation is responsible for introducing smaller roll type structures in deeper and intermediate flow depths. The randomization effect of the smallest flow depth scenario is however strong enough to decimate all local coherence and it makes all flow structures advective. It is interesting to note that the effect of vegetation density dominates over the effect of vegetation flexibility in the sense that when the density is increased, it destroys the roll type structures and makes the flow very

organized by imposing the effect of vegetative drag for the high and intermediate depth cases. This interplay of density and flexibility is also similarly observed on the wave components (not shown). Similar phenomena are also observed in atmospheric and canopy turbulence – where the penetration of low frequency fluctuations inside a canopy are found to depend on wind speed, vegetation cover etc. (Santos et al., 2016). It is important to notice that all POD plots are shown for the same wind speed (W1). The change of wind speed is found to reorganize the energetic modes a little bit without dramatic changes (not shown). Also for the rigid-sparse and rigid-dense cases, vegetative drag
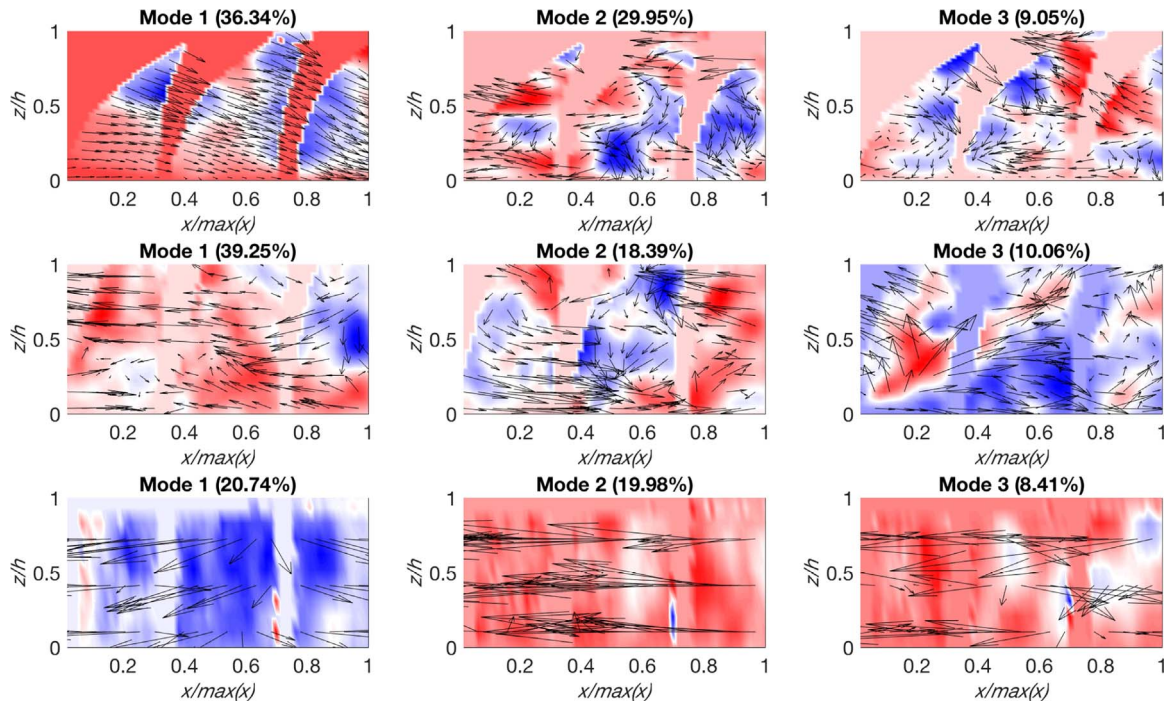

Fig. 6. Same as Fig. 5 – top 3 turbulent POD modes but for the flexible-sparse scenario.
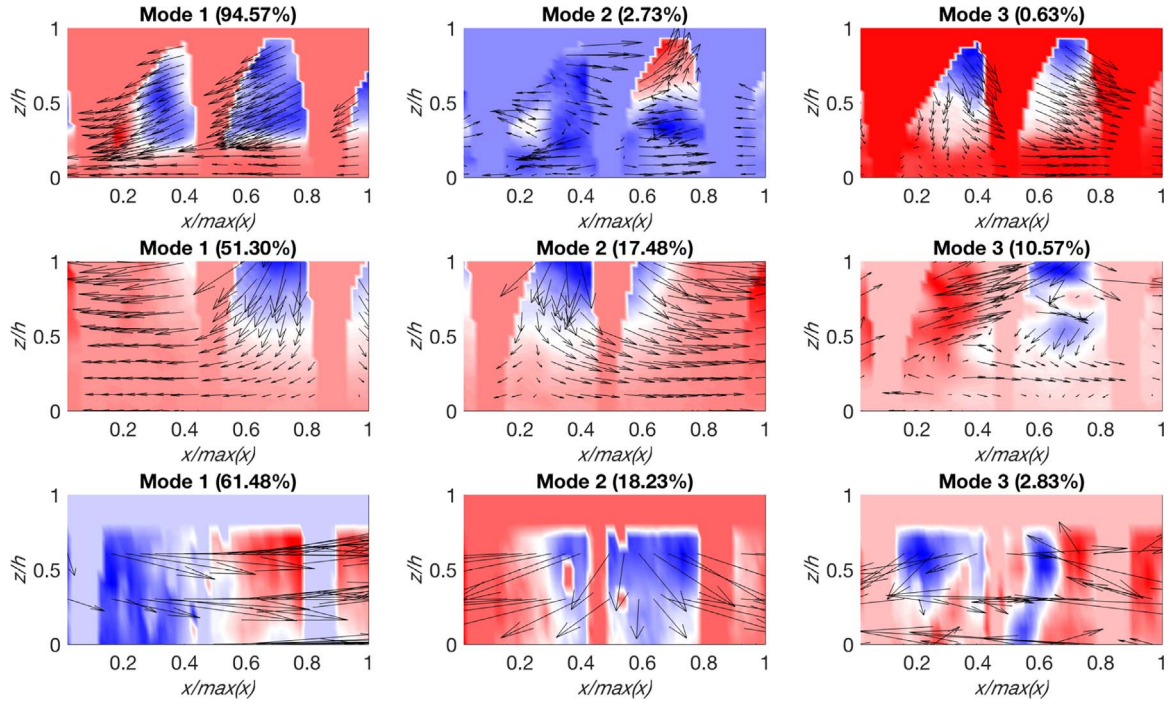
Fig. 7. Same as Fig. 5 – top 3 turbulent POD modes but for the flexible-dense scenario.

is the main difference from the no-vegetation scenario, which introduces more coherence at the smaller flow depths both for wave and turbulence (again, not shown for lack of space). Moreover, another important conclusion from the observation of POD modes for waves and turbulence is that the coherent structures responsible for momentum and energy transport are different. Here it is relevant to mention that similar conclusions were drawn regarding the difference between momentum and energy transport in wind farms by Meyers and Meneveau (2012) using 'momentum and energy tubes'. To further quantify the order and coherence in the wave and turbulence signals, the measures

from information theory are discussed in Section 4.3.

4.3. Variation of Shannon entropy

4.3.1. Observation

Fig. 9 shows spatially averaged vertical profiles of Shannon entropy (S_N) for the turbulent component of the vertical velocity (w) for all HiWj cases and all five scenarios similar to Fig. 2. The u velocity also exhibits similar patterns but the w component is chosen to be shown as more variability is observed in it. Key observations are listed below:
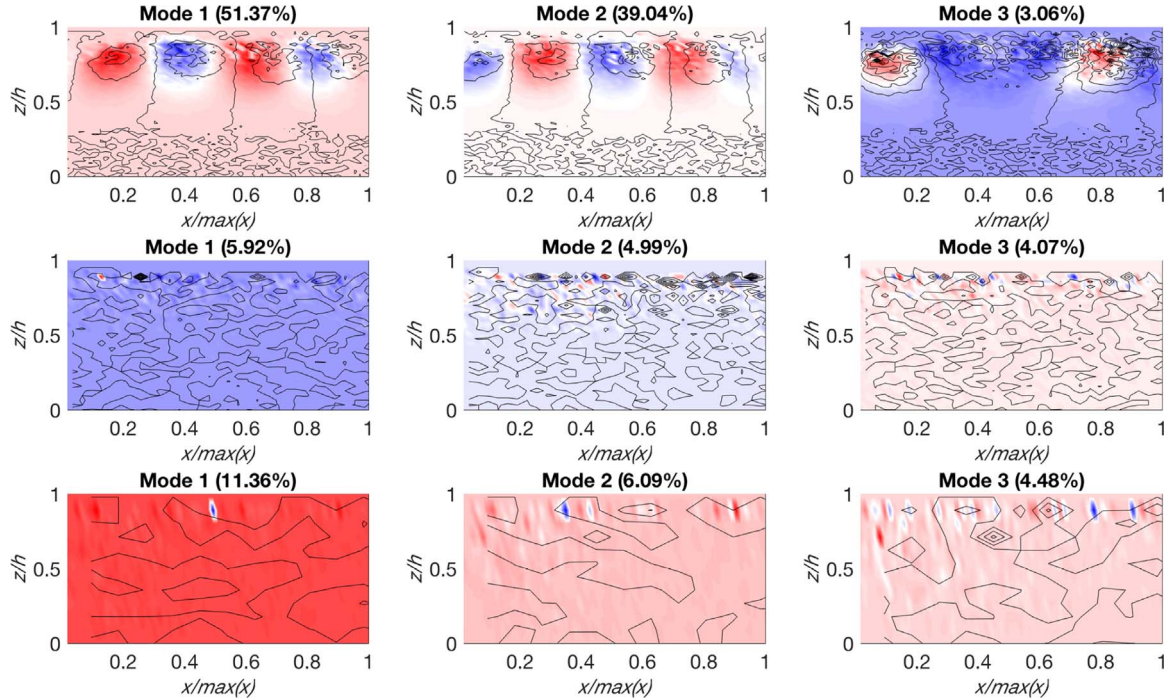

Fig. 8. Similar to Fig. 3 – top 3 POD modes for wave momentum for the no vegetation scenario.
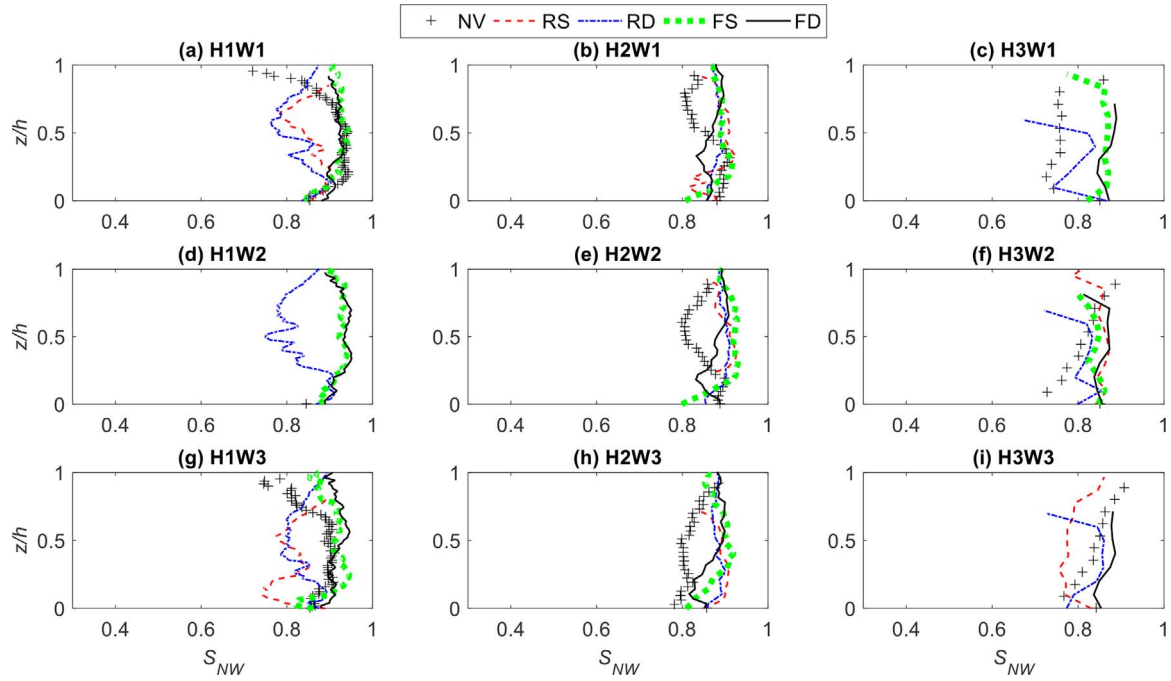
Fig. 9. Similar to Fig. 2 – showing spatially averaged Shannon entropy for the turbulence component of the vertical w velocity.

1 As observed in Fig. 9, for the no vegetation cases, more complex organization in turbulence patterns is observed close to the air--water interface in cases with larger flow depth cases (H1) as apparent from the lower Shannon entropy close.

2 For intermediate and smaller flow depths (H2 and H3), more complex organization is found close to the bottom, especially with the increase of wind speed.

3 For the rigid-dense and rigid-sparse scenarios, a high degree of complex organization is found close to the middle depths and less so close to the interface and bottom for larger flow depths (H1).

4 The flexible sparse and flexible-dense cases, on the other hand, regularizes the flow and increases the entropy in the middle for larger flow depths. For intermediate flow depths (H2), the flexible dense cases reduces the entropy and increases the degree of complexity closes to the middle, which shifts to the bottom with increasing wind speed. The wave components follow similar patterns (not shown).

4.3.2. Discussion

It is interesting to note that the entropy measures can be reconciled with the flow structures revealed by POD in Section 4.2. For example, in Fig. 5, more complex structures are noticed close to the top in the large flow depth case (H1-top row), and the middle and bottom for the intermediate (H2-middle row) and shallow (H3-bottom row) flow depths. This is reflected in the lower entropy (more complex flow structures) close the interface in panels (a), (d) and (g) and lower entropy in panels (b), (e), (h)-and (c), (f), (g) close to middle and bottom in Fig. 9. The fact there is higher level of flow complexity (represented by a lower Shannon entropy) around $0.6h$ can be explained by the fact that the rigid dense vegetation was actually submerged for the H1 (highest) depth cases as described in the experiments section. The top of the rigid vegetation was at the same height and that is responsible for generating inflection type instabilities and rolling structures. Next, to quantify the magnitude of interaction or information exchange between the wave and turbulent components, the mutual information content (MIC) technique is used, which is based on Shannon entropy and is discussed in Section 4.4

4.4. Variation of MIC

4.4.1. Observation

The MIC calculated between the wave and turbulent components of the vertical velocity, for which the spatially averaged vertical profiles are plotted in Fig. 10 for all 5 scenarios for all the HiWj cases similar to Fig. 2. Key observations are as follows:

1 As can be noticed, for the larger flow depths, there is more wave–turbulence interaction close to the air–water interface for the no vegetation scenario. This interaction decreases as water height is reduced and wind speed is increased.

2 With the addition of rigid sparse and rigid dense vegetation, the magnitude of this exchange increases and it becomes maximum in presence of flexible dense vegetation for the deep flow case (H1). For rigid dense vegetation, this interaction is highest around 0.6 h for H1 cases.

3 Increase of wind speed redistributes the nature of this interaction across the flow depths, but reduces the magnitude of this interaction. Especially increase of wind speed seems to push the location of the highest wave–turbulence interaction close to the bottom.

4 The flexible dense scenario always displays high interaction between wave and turbulence. Both for H1 and H2 depth cases, the location of the highest interaction is pushed towards bottom as the wind speed increases. Although for the shallowest (H3) depth scenarios, the interaction seems to be highest close to the very bottom.

4.4.2. Discussion

The most important factor responsible for the variations of wave--turbulence interaction seems to be vegetation flexibility apart from wind speed and of course water height. The dense and flexible vegetation imposes a high drag and tries to organize the flow at middle depths, thus modulating both the wave and turbulence together-so there is more chance to exchange information between them. In general, where the flow is slowed down due to drag effects or generation of more complicated instability induced structures, both wave and turbulence components are affected and that allows more information exchange between them. On the contrary, the air-water interface is characterized by continuous fast passage of wind driven progressive
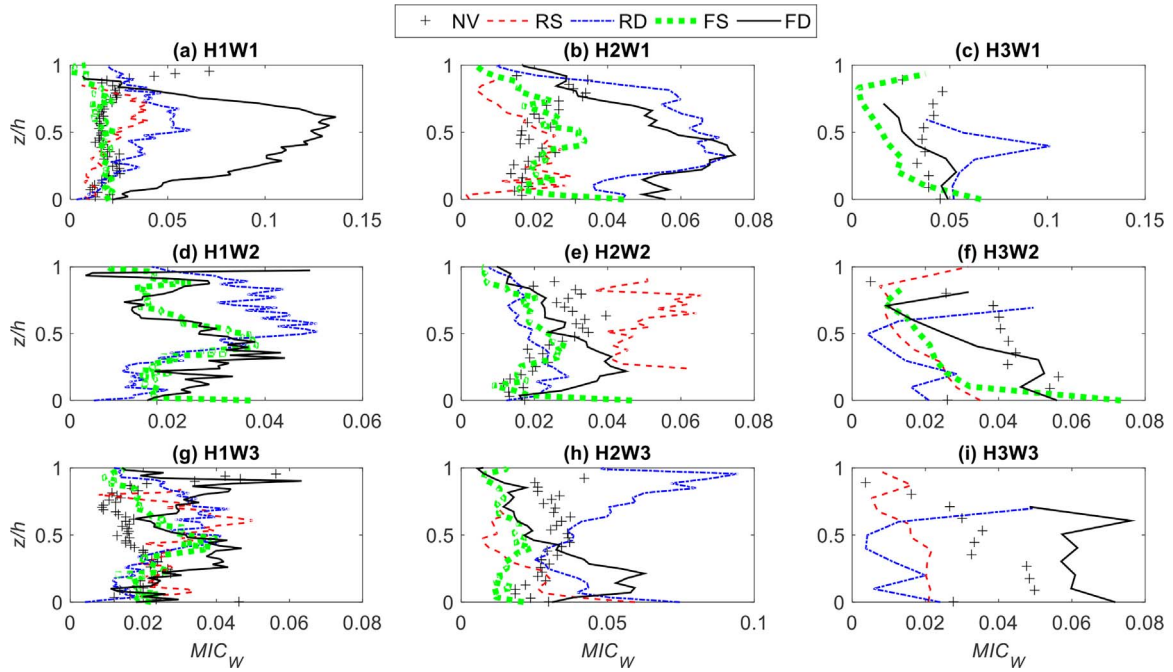
Fig. 10. Similar to Fig. 2 – showing spatially averaged mutual information content between the turbulence and wave components of the vertical w velocity.

waves, allowing less time for interaction between wave and turbulence.

5. Conclusion

The present work has attempted to study coherent structures inside a static water-body under wind shear exhibiting a complex interaction between wave, turbulence and emergent vegetation. PIV experiments were previously conducted by Banerjee et al. (2015) in a flume to study five scenarios such as no vegetation, rigid dense vegetation, flexible sparse vegetation and flexible dense vegetation each for all possible combinations of three different (deep, intermediate and shallow) flow depths and three different (slow, medium, fast) wind speeds. Subsequently data analysis separated wave and turbulence statistics and their variations with different control parameters were studied. Previous instances of such a study involving the full-scale complexity mimicking a realistic natural flow condition in vegetated wetlands could not be found in the literature and it shed new lights on momentum and energy exchange under wave–turbulence–vegetation interaction. To answer the scientific questions mentioned in the introduction, we have employed a suite of different methods, namely quadrant analysis, proper orthogonal decomposition (POD), Shannon entropy and mutual information content (MIC) and have applied them on the separated wave and turbulent components. Our findings to the questions are listed below:

1 To answer question 1, we looked at the difference of momentum transfer from sweeps and ejections. The turbulent component shows either sweep or ejection dominance for momentum transfer, whereas wave momentum transfer is found to have no clear preference for sweeps and ejections. For larger flow depths, vegetation rigidity is found to influence whether turbulent momentum transfer is dominated by sweeps or ejections. For smaller flow depths, the vegetation density appears to be a more influential parameter for the same. The no vegetation scenario is sweep dominated for larger flow depths.

2 Proper orthogonal decomposition (POD) was used to answer question 2. The wave orbital motions can be observed clearly by the top POD modes which show different locations and spans of the most energetic wave components. However, with shallower flow depths,

the wave energy is found to be more distributed and diffused among a large number of POD modes as opposed to a few modes for larger depths, which is also consistent with the deep and shallow wave classification. In general, turbulent motions are found to be more concentrated among the first few modes and less diffused or distributed than wave modes. The dominant modes of momentum transport are found to be different from the dominant modes of energy transfer. The wave orbital motions have less memory or coherence close to the bottom after penetrating the water depth, since they evolve quite rapidly on the air–water interface. Reduction of water depth has a strong effect and the randomization effect of the bottom surface destroys all coherent modes and makes the flow advective. The effect of vegetation flexibility is that it induces several interesting roll type structures, although with increase of vegetation density the drag effect takes over and organizes the flow to become more advective.

3 POD offers a visual clue to answer question 3, but we used Shannon entropy to answer these questions with a more quantitative basis. Flexible and dense vegetation are found to impose a significant amount of coherence by modulating the flow. Vegetation flexibility is found to introduce more interesting and complex vortical structures, whereas vegetation density is found to impose more organization on the flow by means of drag force. The rigid vegetation being submerged generates inflection instability induced structures and complex features as well.

4 To quantify the interaction between waves and turbulence as noted in question 4, we used a measure called mutual information content (MIC) which is based on Shannon entropy. Larger flow depths are found to allow more wave–turbulence interaction, specially for flexible dense vegetation. However, locations where waves or turbulence evolve quite rapidly are found to exhibit less interactions between wave and turbulence such as the air–water interface where the fast and continuous passage of progressive waves allow very little information exchange between wave and turbulence.

It can be concluded that such a combination of methods can unravel the nature of coherent and energetic structures for wave and turbulence, revealing unprecedented details about this complex interaction and other similar flows. These detailed knowledge about the nature of

wave and turbulence are expected to aid model developments by allowing us to develop simple parameterizations capturing the physics of the problem and it will be explored in future works.

Acknowledgments

References

Antonia, R., 1981. Conditional sampling in turbulence measurement. Annu. Rev. Fluid Mech. 13 (1), 131–156.

Banerjee, T., Muste, M., Katul, G., 2015. Flume experiments on wind induced flow in static water bodies in the presence of protruding vegetation. Adv. Water Resour. 76, 11–28.

Berkooz, G., Holmes, P., Lumley, J.L., 1993. The proper orthogonal decomposition in the analysis of turbulent flows. Annu. Rev. Fluid Mech. 25 (1), 539–575.

Calaf, M., Hultmark, M., Oldroyd, H., Simeonov, V., Parlange, M., 2013. Coherent structures and the $k − 1$ spectral behaviour. Phys. Fluids 25 (12), 125107.

Carlin, J.A., Lee, G.-h., Dellapenna, T.M., Laverty, P., 2016. Sediment resuspension by wind, waves, and currents during meteorological frontal passages in a micro-tidal lagoon. Estuar. Coast. Shelf Sci. 172, 24–33.

Caver, D., Meyer, K., 2012. LES of turbulent jet in cross flow. Part 2 – POD analysis and identification of coherent structures. Int. J. Heat Fluid Flow 36 (35), e46.

Chakrabarti, A., Chen, Q., Smith, H.D., Liu, D., 2016. Large eddy simulation of unidirectional and wave flows through vegetation. J. Eng. Mech. 04016048.

Chao, W., Xiu-lei, F., Pei-fang, W., Jun, H., Jin, Q., 2016. Flow characteristics of the wind-driven current with submerged and emergent flexible vegetations in shallow lakes. J. Hydrodyn. Ser. B 28 (5), 746–756.

Chen, H., Reuss, D.L., Hung, D.L., Sick, V., 2013. A practical guide for using proper orthogonal decomposition in engine research. Int. J. Eng. Res. 14 (4), 307–319.

Chen, Y., Li, Y., Cai, T., Thompson, C., Li, Y., 2016. A comparison of biohydrodynamic interaction within mangrove and saltmarsh boundaries. Earth Surface Process. Landf.

Grafteiaux, L., Michard, M., Grosjean, N., 2001. Combining PIV, POD and vortex identification algorithms for the study of unsteady turbulent swirling flows. Meas. Sci. Technol. 12 (9), 1422.

Hu, K., Chen, Q., Wang, H., 2015. A numerical study of vegetation impact on reducing storm surge by wetlands in a semi-enclosed estuary. Coast. Eng. 95, 66–76.

Jin, K.-R., Ji, Z.-G., 2015. An integrated environment model for a constructed wetland-hydrodynamics and transport processes. Ecol. Eng. 84, 416–426.

Katul, G., Poggi, D., Cava, D., Finnigan, J., 2006. The relative importance of ejections and sweeps to momentum transfer in the atmospheric boundary layer. Bound. Layer Meteorol. 120 (3), 367–375.

Kline, S., Reynolds, W., Schraub, F., Runstadler, P., 1967. The structure of turbulent boundary layers. J. Fluid Mech. 30 (4), 741–773.

Kline, S., Robinson, S., 1990. Quasi-coherent structures in the turbulent boundary layer. Part I: status report on a community-wide summary of the data. Near-Wall Turbulence. pp. 200–217.

Lal, A., Moustafa, M.Z., Wilcox, W.M., 2015. The use of discharge perturbations to understand in situ vegetation resistance in wetlands. Water Resour. Res. 51 (4), 2477–2497.

Lumley, J.L., 1967. The structure of inhomogeneous turbulent flows. Atmosp. Turbul.

Radio Wave Propag. 166–178.

Marsooli, R., Orton, P.M., Georgas, N., Blumberg, A.F., 2016. Three-dimensional hydro-dynamic modeling of coastal flood mitigation by wetlands. Coast. Eng. 111, 83–94.

Meyers, J., Meneveau, C., 2012. Flow visualization using momentum and energy transport tubes and applications to turbulent flow in wind farms. arXiv:1209.4578.

Nakagawa, H., Nezu, I., 1977. Prediction of the contributions to the Reynolds stress from bursting events in open-channel flows. J. Fluid Mech. 80 (1), 99–128.

Podvin, B., Fraigneau, Y., 2017. A few thoughts on proper orthogonal decomposition in turbulence. Phys. Fluids 29 (2), 020709.

Poggi, D., Porporato, A., Ridolfi, L., Albertson, J., Katul, G., 2004. Interaction between large and small scales in the canopy sublayer. Geophys. Res. Lett. 31 (5).

Pope, S.B., 2001. Turbulent Flows. IOP Publishing.

Raffel, M., Willert, C.E., Wereley, S., Kompenhans, J., 2013. Particle Image Velocimetry: A Practical Guide. Springer.

Raupach, M., 1981. Conditional statistics of Reynolds stress in rough-wall and smooth-wall turbulent boundary layers. J. Fluid Mech. 108, 363–382.

Robinson, S.K., 1991. Coherent motions in the turbulent boundary layer. Annu. Rev. Fluid Mech. 23 (1), 601–639.

Santos, D.M., Acevedo, O.C., Chamecki, M., Fuentes, J.D., Gerken, T., Stoy, P.C., 2016. Temporal scales of the nocturnal flow within and above a forest canopy in Amazonia. Bound. Layer Meteorol. 1–26.

Shannon, C.E., 1948. A mathematical theory of communications. Bell Syst. Tech. J. 27, 379–623.

Silinski, A., Heuner, M., Troch, P., Puijalon, S., Bouma, T.J., Schoelynck, J., Schröder, U., Fuchs, E., Meire, P., Temmerman, S., 2016. Effects of contrasting wave conditions on scour and drag on pioneer tidal marsh plants. Geomorphology 255, 49–62.

Smith, T.R., Moehlis, J., Holmes, P., 2005. Low-dimensional modelling of turbulence using the proper orthogonal decomposition: a tutorial. Nonlinear Dyn. 41 (1–3), 275–307.

Tambroni, N., da Silva, J.F., Duck, R., McLelland, S., Venier, C., Lanzoni, S., 2016. Experimental investigation of the impact of macroalgal mats on the wave and current dynamics. Adv. Water Resour. 93, 326–335.

Thielicke, W., Stamhuis, E.J., 2010. PIVlab-time-resolved digital particle image velocimetry tool for Matlab. Published under the BSD license, programmed with MATLAB 7 (0.246). pp. R14.

Tirunagari, S., 2015. Exploratory data analysis of the Kelvin–Helmholtz instability in jets. arXiv:1503.06331.

Truong, M.K., Whilden, K.A., Socolofsky, S.A., Irish, J.L., 2015. Experimental study of wave dynamics in coastal wetlands. Environ. Fluid Mech. 15 (4), 851–880.

Tse, I.C., Poindexter, C.M., Variano, E.A., 2016. Wind-driven water motions in wetlands with emergent vegetation. Water Resour. Res.

van Rooijen, A., McCall, R., van Thiel de Vries, J., van Dongeren, A., Reniers, A., Roelvink, J., 2016. Modeling the effect of wave-vegetation interaction on wave setup. J. Geophys. Res.: Oceans.

Wallace, J.M., 2016. Quadrant analysis in turbulence research: history and evolution. Annu. Rev. Fluid Mech. 48, 131–158.

Wesson, K.H., Katul, G.G., Siqueira, M., 2003. Quantifying organization of atmospheric turbulent eddy motion using nonlinear time series analysis. Bound. Layer Meteorol. 106 (3), 507–525.

Wijesekera, H.W., Dillon, T.M., 1997. Shannon entropy as an indicator of age for turbulent overturns in the oceanic thermocline. J. Geophys. Res.: Oceans 102 (C2), 3279–3291.

Yang, Y., 2001. Wind Induced Countercurrent Flow in Shallow Water. University of Western Ontario, London/Ontario, Canada (Ph.D. thesis).

Zhang, M., Qiao, H., Xu, Y., Qiao, Y., Yang, K., 2016. Numerical study of wave-current–vegetation interaction in coastal waters. Environ. Fluid Mech. 1–17.

Zhu, L., Chen, Q., 2015. Numerical modeling of surface waves over submerged flexible vegetation. J. Eng. Mech. 141 (8), A4015001.